

A Morphological and Multicolor Survey for Faint QSOs in the Groth-Westphal Strip^{1,2}

Bernhard Beck-Winchatz³ and Scott F. Anderson

Department of Astronomy, University of Washington, Box 351580, Seattle, WA 98195-1580
bbeck@condor.depaul.edu, anderson@astro.washington.edu

ABSTRACT

Quasars representative of the populous faint end of the luminosity function are frustratingly dim with $m \sim 24$ at intermediate redshift; moreover groundbased surveys for such faint QSOs suffer substantial morphological contamination by compact galaxies having similar colors. In order to establish a more reliable ultrafaint QSO sample, we used the APO 3.5-m telescope to take deep groundbased U -band CCD images in fields previously imaged in V, I with WFPC2/HST. Our approach hence combines multicolor photometry with the $0.1''$ spatial resolution of HST, to establish a morphological and multicolor survey for QSOs extending about 2 magnitudes fainter than most extant groundbased surveys. We present results for the “Groth-Westphal Strip”, in which we identify 10 high likelihood UV-excess candidates having stellar or stellar-nucleus+galaxy morphology in WFPC2. For $m_{606} < 24.0$ (roughly $B \lesssim 24.5$) the surface density of such QSO candidates is $420^{+180}_{-130} \text{ deg}^{-2}$, or a surface density of $290^{+160}_{-110} \text{ deg}^{-2}$ with an additional $V - I$ cut that may further exclude compact emission line galaxies. Even pending confirming spectroscopy, the observed surface density of QSO candidates is already low enough to yield interesting comparisons: our measures agree extremely well with the predictions of several recent luminosity function models.

Subject headings: surveys — quasars: general

¹Based on observations with the NASA/ESA Hubble Space Telescope obtained at the Space Telescope Science Institute, which is operated by the Association of Universities for Research in Astronomy, Inc., under NASA contract NAS5-26555.

²Based on observations obtained with the Apache Point Observatory 3.5-meter telescope, which is owned and operated by the Astrophysical Research Consortium.

³Current address: DePaul University, Department of Physics, Chicago, IL 60614-3504

1. Introduction

The optical $\log N - \log S$ curve and ultimately the luminosity function constrain global models for the evolution of the QSO population (e.g., Schmidt & Green 1983; Hartwick & Schade 1990). The QSO luminosity function has been described via many model parameterizations, but is often characterized as relatively flat at the populous faint end, with a steep fall-off to higher luminosities (e.g., Boyle, Shanks, & Peterson 1988). Physical models for the evolution of the QSO population must explain behavior manifest in the luminosity function and $\log N - \log S$ curve. In turn, the observed luminosity function and $\log N - \log S$ curve may constrain parameters in physically-based evolution models, such as black hole masses, accretion rates, the fraction of galaxies that undergo a QSO phase and the lifetime of this phase, luminosity efficiencies and the role of advection-dominated flows, etc. (e.g., Blandford 1986; Cavaliere & Padovani 1989; Yi 1996; Haiman & Menou 1999).

Despite the impressive depth of well known photographic samples for QSOs which extend to as faint as $B < 22.6$ (e.g., Koo, Kron & Cudworth 1986), there is a need for surveys for even fainter QSOs. Most fundamentally, only ultrafaint QSO samples can provide strong constraints on the faint, populous end of the luminosity function at intermediate to high redshifts. For example, a QSO with $M_B = -22$, i.e., a high space density object from the faint portion of the luminosity function, will have $B \approx 24$ at $z = 2.1$ ($H_0 = 50$ km/s/Mpc, $q_0 = 0$). In order to probe the faint end of the luminosity function, multicolor surveys for ultrafaint QSOs have already been undertaken using groundbased CCD searches alone (e.g., see Osmer et al. 1998 and references therein). The multicolor selection approach is similar to that used by, for example, Koo et al. (1986), and generalized by Warren et al. (1987) to identify even $z > 4$ QSOs.

While such multicolor information is excellent for segregating QSOs from normal stars, a residual uncertainty in groundbased surveys is the difficulty of *morphologically* distinguishing very faint stars/QSOs from very faint galaxies, in the first place. The potential severity of this problem may be realized by noting that there are $\sim 10^2$ times as many galaxies as QSOs per square degree to $m \lesssim 24$; so even a very small fraction of faint contaminating galaxies can dominate uncertainties in QSO candidate selection. Groundbased surveys for ultrafaint QSOs unavoidably suffer from such “morphological” contamination; typical faint field galaxies to $V \lesssim 25$ have a median half-light radius of $< 1''$ (e.g., Roche et al. 1996), and therefore cannot be readily resolved from the ground. Such morphological contamination is likely an obstacle even in current state-of-the-art faint groundbased CCD surveys such as the “Deep Multicolor Survey” (hereafter, DMS; e.g., Hall et al. 1996, Kennefick et al. 1997, Osmer et al. 1998). Follow-up spectroscopy of the DMS candidates extending to $B \sim 22.6$, confirms about 20% of the candidates are in fact QSOs, and the situation at fainter magnitudes in groundbased surveys is likely to be much worse. On the other hand, many moderate-redshift galaxies are by comparison readily morphologically recognizable as resolved objects in *Hubble Space Telescope* (hereafter, HST) images, even beyond $m \sim 24$ (e.g., Griffiths et al. 1994).

We describe a program to obtain a combined morphological and multicolor survey for faint QSOs and related AGNs to $m \lesssim 24$. Our approach is to take deep groundbased u^* -band (similar to U) CCD frames in fields previously imaged in redder $F606W$ and $F814W$ filters from HST. Our survey hence may combine multicolor photometry with the $0.1''$ spatial resolution of HST. While the multicolor aspect of such a survey is well-known and tested from groundbased studies, it is the exquisite morphological information at ultrafaint magnitudes that permits HST to make a new contribution. It should be noted that Sarajedini et al. (1996, 1999ab) have undertaken a morphological survey for low-luminosity AGN searching for resolved galaxies with stellar-nuclei in red $F606W$ and $F814W$ WFPC2 images, although their data set does not include the U -band color information traditionally employed to efficiently select QSOs. Moreover, Conti et al. (1999) and Jarvis & MacAlpine (1999) have recently discussed an approach similar to ours that combines color and HST morphology information. Jarvis & MacAlpine concentrate on high-redshift ($z > 3.5$) quasar candidates in the Hubble Deep Field (HDF), while the Conti et al. study of the HDF also permits an upper limit on the surface density of lower redshift QSOs as well, and thus we discuss the latter results further in §5.

Our paper is organized as follows. We discuss the observations and data reductions in §2, and describe the QSO sample and its selection in §3. We consider some completeness and contamination issues in §4, estimate $\log N - \log S$ curve information in §5 and provide a comparison of our results with extrapolations from brighter existing surveys and predictions based on various luminosity function models. Finally, §6 presents a brief summary and concluding remarks. A more detailed account of much of the information provided herein may be found in Beck-Winchatz (1998).

2. Observations and Reductions

2.1. CCD Observations and Basic Reductions

The most uniform high galactic latitude WFPC2 archival data sets with substantial sky coverage employ $F606W$ and $F814W$ filters. Each WFPC2 field covers 4.4 arc-min^2 , is very deep (better than 10% photometry at $m \approx 25$), and provides superb $\sim 0.1''$ angular resolution. Such red WFPC2 images are available in the archive for several hundred fields at high galactic latitude. Most of these fields are disjoint and widely spread across the sky, but the “Groth-Westphal Strip” (Groth et al. 1994) conveniently and efficiently images a reasonably large adjacent area of sky; this adjacency substantially enhances some aspects of complementary groundbased observations (e.g., see also Koo et al. 1996; Brunner, Connolly, & Szalay 1999).

HST WFPC2 observations of the Groth-Westphal Strip were carried out during March and April of 1994 (Groth et al. 1994), and include a mosaic of 28 slightly overlapping adjacent WFPC2 fields imaged in both $F606W$ (with stacked exposure times of about 2800 s) and $F814W$ (with stacked exposure times of about 4400 s). Bias subtraction, flatfield correction, etc., were performed

by the standard STScI reduction pipeline. Cosmic ray removal and coaddition of the 4 separate exposures in each WFPC2 field and bandpass were carried out by the authors. No correction for the charge-transfer efficiency (CTE) problem was applied, since the error introduced is expected to be small (e.g., Holtzman et al. 1995). Vignetted regions of the WFPC2 images were trimmed before analysis.

The *F606W* and *F814W* filters alone do not provide adequate color information to efficiently select quasar candidates, so we obtained complementary bluer CCD images of the Groth-Westphal Strip, remotely using the 3.5-m Apache Point Observatory (APO) telescope (owned and operated by the Astrophysical Research Consortium) in New Mexico. The APO 3.5-m data discussed here were taken with the Seaver Prototype Imaging CCD camera (hereafter SPIcam), using a filter which we refer to here as u^* ; this filter is similar to the Sloan Digital Sky Survey (SDSS) u' filter (e.g., Fukugita et al. 1996). SPIcam is a backside illuminated SITe 2048² pixel device with 24 μ pixels, and a plate scale of 0.28'' per pixel with 2 \times 2 binning. Bias subtraction, flatfield correction, trimming, and cosmic ray removal were performed in standard fashion. The SPIcam field of view can capture most (about 90%) of 3 adjacent WFPC2 fields in a single image, and our survey region concentrates on 24 adjacent WFPC2 fields of the Groth-Westphal Strip, which we have also imaged in 8 u^* SPIcam fields. (Our survey region does not include the four most NE WFPC2 fields of the Strip). Typically, each of the 8 SPIcam fields was observed in u^* with a total exposure time of about 8000 s.

Our survey area has a complicated geometry of partially overlapping WFPC2 and SPIcam fields. We calculate the survey region to be 0.0245 deg² by projecting the WFPC2 fields onto the SPIcam fields, and adding up all SPIcam pixels which overlap an unvignetted portion of at least one WFC field (accounting for areas covered more than once).

2.2. Object Detection and Photometry in Stacked CCD Frames

Object detection in the stacked WFPC2 images was performed with SExtractor V1.2 (Bertin & Arnouts 1996), generating a catalog of about 6700 objects; detection completeness is very high to our survey magnitude limits (see §4.1). The Groth-Westphal Strip is at high Galactic latitude, and since crowding is not a problem, aperture photometry was obtained for all objects using a 3 pixel radius aperture. Aperture corrections were performed according to the prescription by Holtzman et al. (1995). Zeropoints for the Vega magnitude system were taken from Whitmore (1995). The HST Medium Deep Survey project (hereafter MDS; Ratnatunga, Griffiths, & Ostrander 1999) has electronically published a catalog of objects in the Groth-Westphal Strip which includes “total maximum likelihood estimation” *F606W* and *F814W* magnitudes for each object. The MDS catalog thus provides an independent check on the WFPC2 detection, photometry, and morphological classification algorithms we employ (see below). For stellar-PSF objects within our survey limits of $19.3 < m_{606} < 24.0$, we find excellent agreement between our photometry and that of the MDS: $m_{606}^{ap} - m_{606}^{mds} = 0.09 \pm 0.11$, and $(m_{606} - m_{814})^{ap} - (m_{606} - m_{814})^{mds} = 0.03 \pm 0.10$,

where the superscripts ap and mds denote our aperture photometry and MDS photometry, respectively.

Object detection in the groundbased u^* SPIcam images was also performed with SExtractor, generating a catalog of about 1700 objects (see §4.1 for quantification of detection completeness). Instrumental magnitudes for all SPIcam detected objects were calculated in a $2.8''$ diameter aperture; aperture corrections were estimated using the 4-5 brightest unsaturated stellar-PSF objects in each stacked image and should be accurate to <0.05 magnitudes. Calibration to a u^* system similar to the expectations for the eventual u' SDSS system (the SDSS system is currently being carefully defined) were carried out via observations of Feige 34, Feige 66, BD +26° 2606, and BD +33° 2642, and a number of Landolt standards (using approximate transformations in Fukugita et al. 1996), and adopting $u^*=10.78$ for BD+26° 2606.

Astrometric information is available for the WFCP2 images via the STScI pipeline reductions; a small correction was made to the astrometric information in the original headers using the *STSDAS* script called ‘uchcoord’ (version 1.1). An astrometric solution was also derived for each stacked SPIcam image using the Digitized Sky Survey. Objects detected in both WFCP2 and SPIcam images, whose positions agreed (before corrections) to better than $2''$, were used to place the two data sets on the same astrometric frame. After correction, the mean deviation between positions of stellar-PSF objects derived from WFPC2 versus SPIcam frames is $0.4''$.

3. Sample Selection

The terminology “quasi-stellar” of course traditionally has implied approximately stellar morphology in groundbased images. The morphological discrimination in groundbased images of bright stars and QSO candidates on the one hand from bright galaxies on the other is relatively straight-forward. However, faint field galaxies typically have half-light radii $< 1''$ (e.g., Roche et al. 1996) and cannot readily be resolved from the ground. Our survey aims to reduce the morphological contamination inherent in deep groundbased multicolor surveys by taking advantage of the $0.1''$ resolution of HST/WFPC2 images in the survey region. Broadly speaking, our method is to select and then merge two subsamples of UV-excess QSO candidates. We first select a sub-sample of QSO candidates consisting of UV-excess objects with $19.3 < m_{606} < 24.0$ that are unresolved (i.e., have stellar-PSF morphology) in the WFPC2 images. Then as the host galaxies of QSOs may be resolved at the angular resolution of HST (e.g., Hutchings et al. 1994; Bahcall et al. 1997; Hooper et al. 1997), we also separately select UV-excess objects that appear to have stellar-PSFs in our *groundbased* SPIcam images, and then further examine their morphology in detail in the WFPC2 images; we ultimately retain in the second subsample only those objects whose morphology based on quantitative criteria is consistent with an approximately unresolved (stellar-PSF) nucleus in WFPC2, even if an underlying galaxy is also evident. Our final QSO sample consistently merges candidates from these two UV-excess sub-samples.

3.1. QSO Candidates with Stellar-PSF Morphology in WFPC2

We first select objects having stellar morphology in WFPC2 via application of the SExtractor software to the 72 stacked WFC images of our survey region of the Groth-Westphal Strip. SExtractor, which uses a neural network for stellar-PSF vs. galaxy separation, outputs a “stellarity index” for each object. This index is 0.0 and 1.0 for objects that are confidently identified as galaxies and stars, respectively; more ambiguous objects are assigned values close to 0.5. An input parameter to SExtractor that influences this output stellarity index is a user-specified FWHM of stellar-PSF objects. We estimate an appropriate input FWHM iteratively. We start by fitting a Gaussian to a few high signal-to-noise stellar (in WFPC2) objects to determine a representative FWHM. All 72 WFC images are then analyzed with SExtractor using this initial input FWHM value. We then fit a Gaussian to all objects with a stellarity index greater than 0.5 and use the median FWHM of Gaussian fits from that iteration to reanalyze the images once again with SExtractor, etc. This process is repeated iteratively and converges to finally adopted SExtractor input FWHM values of 1.48 pixels for *F606W* images and 1.60 pixels for *F814W* images. We verify that these are reasonable values first by visually confirming that high signal-to-noise stars and galaxies, and low signal-to-noise ambiguous objects are finally assigned stellarity indices close to 1.0, 0.0, and 0.5, respectively. Objects with SExtractor stellarity indices greater than 0.5 in both WFPC2 filters are ultimately considered morphologically “stellar” in our sample. Second, we appeal to an entirely independent morphology algorithm as described below as a further quantitative check that we have not missed truly stellar-PSF objects.

Shown in Figure 1 is a two-color diagram of objects with $19.3 < m_{606} < 24.0$ found to have stellar morphology in *F606W* and *F814W* WFPC2 images according to the SExtractor analysis. For added clarity in Figure 1, we have not displayed data for non-detections in u^* (with one exception discussed below), although objects with such limits are accounted for in our analyses. It is reassuring that the bulk of the objects in this two-color diagram appear to indeed comprise a “stellar sequence”, empirically confirming that the morphological criteria employed have excluded most galaxies. A handful of odd-color outliers, including quasar candidates (solid symbols) having stellar-morphology in WFPC2, and perhaps a few still-unresolved compact galaxies, are also evident in Figure 1; we discuss these below.

Figure 2 duplicates the data in Figure 1, except that we also overplot for approximate comparison the synthetic colors expected for main sequence stars M8 through F8 (5-point star symbols in Figure 2). To generate these synthetic points, we use the Gunn & Stryker (1983) catalog and *SYNPHOT* to convolve catalog spectrophotometry with the wavelength dependent sensitivity curves of WFPC2 *F606W/F814W* and an approximate u^* sensitivity curve. There is a reasonably good match between observed and synthetic stellar sequences, especially as the u^* sensitivity curve is only an approximate prediction; for example, the available u^* transmission curve is actually for a different detector and telescope, the low metallicity expected for halo stars has not been accounted for, etc. There appear to be few main sequence stars earlier than early-G/late-F in our “stellar” sample as might be predictable for faint halo stars; indeed a clump

of likely low-metallicity Galactic halo subdwarfs appears as expected near $(m_{606} - m_{814}) \sim 0.55$, but more ultraviolet than the main sequence. For additional rough comparison, we also show in Figure 2 the colors expected for a “typical” QSO at various redshifts (solid curve). We estimate these colors using the composite spectrum derived from 700 QSOs of the Large Bright Quasar Survey (LBQS; Francis et al. 1991), redshifted and convolved with the approximate u^* , $F606W$, and $F814W$ sensitivity curves. As may be verified in this figure, typical QSOs with redshifts $z < 2.1$ appear more ultraviolet in $(u^* - m_{606})$ than normal stars.

Traditional UV-excess surveys have selected objects with $(U - B) < -0.4$, a criterion often thought to recover about 95% of $z < 2.2$ QSOs (Veron 1983); at larger redshifts Ly- α leaves the U -band and enters the B -band, with $(U - B)$ becoming redder rapidly and assuming the values of normal stars. The red edge of the u^* -filter we use is at a slightly shorter wavelength than the red edge of the U -band, and consequently our redshift limit is slightly lower at about $z \lesssim 2.1$. We adopt a UV-excess limit of $(u^* - m_{606}) < 0.7$ for QSO candidate selection; for reference this limit is shown by the horizontal dotted line in Figures 1–2. Note that near the $m_{606} < 24$ survey limit there are red objects not detected in u^* , but none of these non-detections have limits in $(u^* - m_{606})$ which satisfy our UV-excess criterion; in part, a desire to avoid such complications motivates the choice of our survey limit of $m_{606} < 24.0$.

The four QSO candidates that meet our criteria (UV-excess and unresolved stellar morphology in WFPC2 according to SExtractor) are marked by solid circles in Figures 1–2, and are listed in the first four rows of Table 1. Upon visual examination of the WFPC2 images, the candidate we catalog as #98 does appear to have an associated underlying galaxy. However, the dominant nucleus certainly appears stellar; moreover, this object also satisfies a third set of quantitative morphology criteria discussed in §3.2., and therefore is appropriately retained in the final sample in any case.

As noted above, the Medium Deep Survey project (Ratnatunga et al. 1999) has developed two-dimensional maximum likelihood image analysis software and previously applied it to the WFPC2 images of the Groth-Westphal Strip. Because their algorithms for detection and morphological star-galaxy separation are entirely independent of the above SExtractor neural network approach, the electronic MDS catalogs provide a valuable cross-check on our analyses. Objects in the MDS algorithms are morphologically classified as stellar, disk, bulge, or disk+bulge (MDS classes 0, 1, 2, and 3). All 165 objects in our survey area, and within our survey magnitude limits, which are classified in the MDS catalogs as morphologically stellar in both the $F606W$ and $F814W$, are also classified as morphologically stellar by our SExtractor analysis. Our SExtractor analysis classifies a few more (about 5%) objects as “stellar” in WFPC2 than the MDS catalogs, so our SExtractor classifications in WFPC2 appear robust but slightly more inclusive than the MDS ones. The excellent agreement between SExtractor stellar-PSF classifications and those of the MDS confirms the efficacy of both approaches. All UV-excess QSO candidates with stellar morphology in WFPC2, were already identified via the SExtractor neural network approach; that is, no additional QSO candidates with stellar morphology and having UV-excess are added from

consideration of objects independently classified as “stellar” in the MDS catalogs.

We also call attention to two non-UV-excess objects (solid squares in Figures 1–2) with stellar-PSF morphology in WFPC2, whose unusual colors fall markedly above the stellar sequence and close to the colors predicted for $z \sim 3$ QSOs. We list these miscellaneous higher-redshift QSO candidates in the last two rows of Table 1, but of course do not include them in our UV-excess sample.

3.2. QSO/AGN Candidates with Stellar-Nuclei in WFPC2, but having Resolved Underlying Galaxies

As noted above, HST studies show that some QSOs with stellar morphology in groundbased images have resolved host galaxies when observed at WFPC2 spatial resolution. QSOs with such host galaxies would not necessarily have been classified as morphologically stellar by either the SExtractor neural network or the MDS algorithms applied to WFPC2 images as described in §3.1. Our strategy to find such QSOs with underlying host galaxies is to initially identify UV-excess objects that are approximately stellar in *groundbased* images, and then consider their morphology in more detail using the HST images. Ultimately, we will select a subsample of these UV-excess objects for which the nucleus is approximately stellar, even if an underlying galaxy is also evident in WFPC2.

For the initial stages of the selection of this second subsample, we again use morphology information from SExtractor, but this time applied to the stacked u^* SPIcam groundbased images. Again, the quality of the star-galaxy morphology separation depends on the value input to SExtractor for the FWHM of stellar objects. As seeing in the groundbased images differs from field to field, we estimate input FWHM values for each stacked SPIcam image separately, using the median FWHM of the ~ 10 brightest stellar objects in each stacked image. The adopted input FWHM’s vary between 5.0 and 6.6 pixels ($1.4''$ - $1.9''$), and we verify that the neural network assigns reasonable output stellarity indices by confirming that high signal-to-noise galaxies and stars, and low signal-to-noise ambiguous objects, are assigned values close to 0.0, 1.0, and 0.5, respectively.

The positions of UV-excess objects detected in the u^* groundbased images are matched to our catalogs of objects detected in the redder WFPC2 filters. In our survey area, we find 77 objects that have UV-excess, $19.3 < m_{606} < 24.0$, and SExtractor stellarity indices > 0.5 in the stacked *groundbased* u^* images. Although these UV-excess objects are stellar in the groundbased images (i.e., a traditional definition of “quasi-stellar”), an initial visual examination of the 77 UV-excess candidates shows that most (80%) are readily resolved into galaxies on the WFPC2 images, confirming the likely severity of morphological contamination of ultrafaint QSO surveys that rely entirely on groundbased imaging data. Because many of the objects selected in this fashion turn out to be extended in WFPC2, we initially consider their MDS “total magnitudes” in $F606W$ and $F814W$. Such model magnitudes may be preferred to WFPC2 aperture magnitudes

for some extended objects, although when we later confine our attention to just that subset of the objects with stellar-nuclei in WFPC2, we will return to small-aperture magnitudes for the nuclei.

In order to establish an objectively-selected sub-sample, we employ quantitative morphological tests to select QSO/AGN candidates having a compact approximately-stellar nucleus, but resolved host galaxy in WFPC2. These morphological tests consist of two parts. The first part is designed to exclude UV-excess galaxies whose nuclei are significantly more extended than typical stellar-PSF objects in WFPC2. We calculate a normalized integrated and azimuthally-averaged radial profile parameter I_{RAD} for the core of each of the 77 initial UV-excess objects. We measure the $F606W$ -fluxes through apertures of radii of one, two, and three pixels and divide these by the total flux of the object measured at an aperture radius of 14 pixels. For comparison, a template radial profile typical of truly stellar objects is derived by averaging the similarly measured and normalized fluxes of the high signal-to-noise ($m_{606} < 21$) stellar objects (as classified by SExtractor) in the WFPC2 images. We then integrate the area between this template profile for stellar-PSF's and each object's core profile (this is the parameter I_{RAD}), and exclude all objects for which the integral is larger than a certain threshold value. We select a threshold value based on the observed distribution (Figure 3) of the integral values I_{RAD} for stellar-PSF objects (as classified by the neural network in WFPC2) to the magnitude limit of the survey. With our adopted value of $I_{RAD} < 0.5$, all but one of the objects classified by SExtractor as having stellar-PSF morphology in WFPC2 would have passed our I_{RAD} test.

A second morphological test is needed however, as some very compact UV-excess objects that are slightly elongated in WFPC2 images pass the first I_{RAD} radial profile test described above; in part, this is due to the azimuthal averaging with I_{RAD} . Yet UV-excess objects with such compact elliptical morphology are most likely compact narrow emission line galaxies (or CNELG's), which are known to be the major contaminant of groundbased surveys for faint QSOs (e.g., Koo & Kron 1988; Hall et al. 1996). We therefore also then test the roundness of UV-excess objects (which pass the I_{RAD} test) in WFPC2 by fitting two-dimensional Gaussians to their profiles. Objects for which the major to minor axis ratio R_{MAJ}/R_{MIN} of the best-fit Gaussian falls above a certain threshold are also morphologically excluded from the final QSO candidate sample. We base the value of this threshold on the observed distribution (Figure 4) of major to minor axis ratios of the stellar-PSF objects selected by SExtractor. With our adopted value of $R_{MAJ}/R_{MIN} < 1.5$, every object classified by SExtractor as having stellar-morphology in WFPC2 would have passed this second ellipticity test.

Table 2 lists the seven UV-excess objects initially classified by SExtractor as having stellar morphology in our *groundbased* images, which also pass both our I_{RAD} and R_{MAJ}/R_{MIN} morphology tests in WFPC2 frames. We list in Table 2 only the additional QSO/AGN candidates found in this fashion, and do not repeat those from Table 1 (which have stellar morphology in WFPC2, and so also satisfy the I_{RAD} and R_{MAJ}/R_{MIN} criteria). The objects in Table 2 are QSO/AGN candidates with approximately stellar-nuclei, even if they have resolved host galaxies in WFPC2. Their location in the two color diagram is shown in Figure 5 (see filled circles); note

that other data in Figures 1 and 5 are quite similar, except that Figure 5 displays MDS catalog $F606W$ and $F814W$ magnitudes.

Table 3 lists other miscellaneous UV-excess objects that fall near to, but somewhat outside, the parameter space of our QSO/AGN selection criteria. This miscellaneous list includes mainly UV-excess objects we might have identified as possible QSO candidates via a simple visual examination of the WFPC2 images but which fail the quantitative morphology tests, plus one UV object (#1176) that meets the morphology criteria but is slightly fainter than the magnitude limit of the survey. We do not consider these miscellaneous objects further in the current paper.

3.3. The Combined Samples of QSO/AGN Candidates

Our combined sample of QSO candidates—called Sample I—is conceptually the merging of UV-excess objects selected in §3.1 and 3.2 and listed in Tables 1 and 2, and includes objects with stellar morphology in WFPC2, as well as objects with approximately-stellar nuclei in WFPC2 even if the underlying host galaxies are resolved. However, for greater consistency with the stellar-PSF objects selected in §3.1, in combining the subsamples from §3.1 and §3.2 we henceforth consider only the small-aperture WFPC2 photometry. As quantified above, there is excellent agreement between our aperture measures and the MDS “total magnitudes” for point sources, but the total MDS magnitudes for the stellar-nucleus + galaxy QSO candidates discussed in §3.2 tend to be slightly brighter than our WFPC2 aperture magnitudes. Even so, this small systematic difference in photometry for extended objects effectively eliminates only the QSO candidate #72 in Table 2 from further consideration in the merged Sample I: its small-aperture magnitude slightly exceeds $m_{606} = 24.0$, although the MDS total magnitude is 23.9.

The QSO candidates in Sample I are chosen according to the following criteria: aperture magnitudes $19.3 < m_{606} < 24.0$, $(u^* - m_{606}) < 0.7$, and either (a) SExtractor stellarity indices >0.5 in $F606W$ and $F814W$ images, or (b) SExtractor stellarity index >0.5 in u^* groundbased images, and meeting integral I_{RAD} and roundness R_{MAJ}/R_{MIN} criteria for stellar-nuclei objects in WFPC2. Table 4 provides merged summary information for the 10 QSO candidates of Sample I.

As discussed earlier, compact narrow emission line galaxies (CNELG’s) are known to have $(U - B)$ colors similar to those of $z \lesssim 2$ QSOs but often with somewhat redder $(B - V)$ indices. They are a major contaminant of groundbased surveys for faint QSOs. Some other multicolor surveys thus have attempted to reduce this contamination by excluding UV-excess objects redder than a certain $(B - V)$ from their candidate list. For example, Hall et al. (1996) apply a magnitude dependent cut-off value $(B - V)=0.25-0.4$, while Koo et al. (1986) exclude objects with $(J - F) >0.55$. We have already attempted to exclude CNELG’s on the basis of their morphology, but to reduce residual contamination we also devise a second sample—which we call Sample II—with a red limit on the $(m_{606} - m_{814})$ color, in addition to the UV-excess and morphology criteria described above. Using synthetic photometry applied to the LBQS composite QSO

spectrum redshifted through the range $z=0.5-2.1$, we estimate $\langle m_{606} - m_{814} \rangle \approx \langle B - V \rangle + 0.2$. We thus adopt a red limit of $(m_{606} - m_{814W}) < 0.55$ for Sample II, corresponding to $(B - V) \lesssim 0.35$ for typical QSOs. Sample II includes seven objects: three QSO candidates, #1148, 507, and 245, from the full Sample I are redder than this $(m_{606} - m_{814})$ limit, and are excluded from Sample II.

4. Some Completeness and Contamination Issues

As we will show §5, the surface density of *candidates* we find is extremely well matched to expectations for QSOs based on extrapolations from surveys at brighter magnitudes, and predictions of various model luminosity functions; this suggests the possibility of high completeness and low contamination in our sample, although definitive confirmation must await follow-on spectroscopy. The completeness of UV-excess selection is addressed by many other studies (e.g., Veron 1983) and as noted above is generally thought to be 90–95% for $z \lesssim 2.2$ QSOs (but see Graham, Clowes, & Campusano 1998 for an alternate view). Here we address a few other issues bearing on completeness/contamination.

4.1. Detection Completeness

We use Monte Carlo simulations to establish the completeness of the SExtractor detection algorithm as a function of u^* magnitude in our groundbased SPIcam images. This is relevant for QSO/AGN candidates selected in §3.2. Artificial “stellar” (in 1.6” groundbased images) objects of known magnitudes are added to these SPIcam images, which are then reanalyzed using SExtractor. The PSF of the artificial objects is modeled using the brightest actual stellar objects in each field. We detect ~ 80 “stellar” objects to $u^*=25$ in a typical SPIcam field, and find that adding 8 artificial objects per field does not significantly alter SExtractor detection or classification of the real objects. A total of 288 artificial objects per 0.^m1 bin were created between $u^*=23.0$ and $u^*=25.0$ and added to each of the stacked SPIcam images. Positions of artificial objects on the stacked SPIcam frames were assigned by a random number generator. Poisson noise was added to the artificial star template PSF, while readnoise and background noise are already accounted for by adding the artificial objects to the existing CCD images. The artificial images were then analyzed with SExtractor in the same manner as the real data. All 8 of our stacked SPIcam images reach similar depths. We show in Table 5 the detection probabilities based on these tests. (We did not perform extensive Monte Carlo simulations for $20 < u^* < 23$, but expect detection probabilities > 0.97 by extrapolation from our simulations at $u^* > 23$). Our survey limit of $m_{606} < 24.0$ is also chosen to insure that SPIcam u^* detection completeness typically exceeds about 50% even for the least UV-excess objects that might potentially enter the sample at the survey limits (and for the bulk of the sample objects, detection completeness in u^* images is in the 80-90% regime).

Both our own completeness tests for our SExtractor derived WFPC2 catalogs, and tests independently carried out by the creators of the MDS catalogs (Ratnatunga et al. 1999), confirm that object detection in the even deeper WFPC2 images is nearly 100% complete to at least a half-magnitude fainter than our survey limit. Thus, no completeness corrections are made for those UV-excess QSO candidates (discussed in §3.1 and listed in Table 1) initially selected from the catalogs of WFPC2 objects having stellar morphology.

4.2. Contamination by Stars

While the major contaminant of UV-excess quasar surveys at bright limiting magnitudes are galactic stars (e.g., hot white dwarfs and low-metallicity subdwarfs), deeper UV-excess and multicolor QSO surveys with confirming spectroscopy show that to $B \sim 22.5$ stars are generally minor contaminants. For example, in the multicolor selected sample of QSO candidates in SA57 (Koo et al. 1986; Koo & Kron 1988), 10% and 15% of the candidates at $B \leq 22$ are respectively white dwarfs and subdwarfs, while at $B > 22$ these stars make up only 4% and 7% of the candidates, respectively. At most, only 3 of 10 of our UV-excess candidates might be stars, and indeed one of these three objects, #245, may also weakly show evidence for a host galaxy in *F814W*; the other 7 candidates in Sample I are morphologically resolved according to the algorithms and/or in a visual examination of the WFPC2 images.

It is unlikely that all three potentially stellar in WFPC2 QSO candidates (#971, 815, and 245) are white dwarfs. The absolute magnitudes of disk white dwarfs may be estimated from their colors (Fleming et al. 1986) as $M_V \sim 11.9 + 2.9(U - V) - 0.5(U - V)^2$. We estimate $(U - V) \sim -0.4$ for #971 and ~ -0.7 for #815 and #245, using synthetic photometry to approximately convert between our magnitudes and the Johnson system. Thus candidates # 971, 815, and 245 would have $M_V \approx 10.7, 9.6,$ and $9.6,$ respectively, were they white dwarfs. Assuming a disk scale height for white dwarfs of $\lesssim 500$ pc, one might expect $d \lesssim 1000$ pc for disk white dwarfs toward the Groth-Westphal Strip ($b=60^\circ$). However, the apparent magnitude of a white dwarf with $M_V=9.6$ seen at a distance of 1000 pc is $V \approx 19.6$, and therefore candidates #815 and #245 are much too faint to be disk white dwarfs. The object cataloged as ID #971 would be at a more plausible (although still distant) ~ 600 pc above the galactic plane; and it is not inconceivable to expect $\lesssim 1$ disk white dwarf in our survey area. Assuming $d \lesssim 1000$ pc and for our survey area of 0.025 deg^2 , we sample a volume of the disk for white dwarfs of $\sim 2500 \text{ pc}^3$. The space density of hot white dwarfs to $M_V < 11.25$ is $\sim 1.5 \times 10^{-4} \text{ pc}^{-3}$ (Liebert, Dahn, & Monet 1988), and hence, the total number of hot (UV-excess) disk white dwarfs expected in our survey is $\lesssim 0.4$. (see also Gould, Flynn, & Bahcall 1998).

One might also entertain some possibility that #815 and #245 are very distant white dwarfs. Objects having the $(u^* - m_{606})$ colors of #815 and #245, were they similar to disk white dwarfs, would be at ~ 8 kpc and well into the halo. However, on rather general grounds, it might be surprising to find a significant population of very blue white dwarfs abundant in the halo

population (although see Beck-Winchatz 1998 for further discussion, and e.g., Hansen 1998).

Contamination by subdwarfs is difficult to dismiss. The subdwarf clump near the location of late-F/early-G stars with bluer ($u^* - m_{606}$) colors than main sequence stars appears to be evident in our two-color diagrams (e.g., Figure 1). All stellar-PSF QSO candidates in our sample are more UV-excess than this clump. It seems unlikely these QSO candidates are actually subdwarfs, but follow-on spectroscopy is certainly desirable to confidently confirm their nature.

4.3. Morphological Contamination and Incompleteness

Central to our approach is the use of HST morphology information to select a subset of the UV-excess objects that have either stellar-PSFs or which have resolved galaxies with approximately stellar-nuclei; this morphological selection should (and appears to) eliminate a large fraction of the compact galaxies that contaminate groundbased surveys for faint QSOs. However, there may of course still be some residual contamination by extremely compact galaxies inadequately resolved even at HST resolution. We have attempted to further reduce such contamination by generating Sample II which excludes three Sample I objects on the basis of their red ($m_{606} - m_{814}$) color. However, a full assessment of the contamination of our sample by non-active galaxies awaits spectroscopic follow-up.

As noted above, among the objects with apparently stellar PSFs in our *groundbased* images there are 77 which have a UV-excess. One might also consider if within this group there are a significant number of QSOs ultimately excluded by our WFPC2 morphology criteria of §3.2. One indication that this is unlikely to be a major (e.g., more than $2\times$) effect is provided in the recent HST study by Malkan, Gorjian, & Tam (1998) of the morphology of nearby Seyferts as revealed by WFPC2 images. Among nearby Seyfert 1 galaxies, Malkan et al. find that only 37% show no discernible point sources, or have point sources which contribute less than $\sim 45\%$ of the light within the inner one arc second. Nonetheless, the Malkan et al. study leaves open the possibility that some of the UV-excess objects lacking PSF-nuclei in WFPC2 (which we have excluded from our samples) are in fact QSOs or Seyferts 1s. Thus, spectroscopic follow-up of some of these morphologically excluded objects would also be useful.

5. Surface Density of Ultrafaint QSO/AGN Candidates

While the luminosity function provides a more direct test, many checks of statistical and physical models of QSO evolution can be made using observed number-magnitude relations alone. Here we derive the $\log N - \log S$ curve for QSO *candidates* to $m < 24$. Pending confirming spectroscopy, of course, we cannot be sure that our candidates are indeed QSOs/AGNs. However as we now show, our derived QSO candidate surface density at ultrafaint magnitudes is sufficiently low to already provide interesting comparisons with extrapolations from the $\log N - \log S$ curve of

brighter quasars, as well as various model luminosity function predictions.

While our survey is $F606W$ magnitude limited, most existing QSO surveys define magnitude limits and quote surface densities in terms of Johnson B magnitudes. In order to roughly compare our results with those other surveys, we thus first derive an approximate transformation from $F606W$ magnitudes to the B -band (Figure 6). We model a typical QSO spectral shape by fitting a cubic spline to the continuum windows identified by Francis et al. (1991) at 1285, 2200, 4200, and 5770 Å for the LBQS composite spectrum. Then both the LBQS composite spectrum itself and the continuum fit are numerically redshifted and convolved with the $F606W$ and B -bandpasses, to yield a rough conversion between observed (with emission lines) $F606W$ magnitudes and continuum (without lines) B -band magnitudes. This conversion, $(m_{606} - B)$, as a function of redshift is shown in Figure 6. Since the $F606W$ and B passbands cover markedly different wavelength ranges, the derived transformation is highly dependent on the assumed spectrum and should not be used for any objects except for $z \lesssim 2.1$ QSOs, and even then only for rough comparison. Since we do not know the redshifts of the QSOs among our candidates, we adopt a typical transformation of $B \approx m_{606} + 0.5$.

Table 6 shows the cumulative surface densities implied by our QSO survey at ultrafaint magnitudes. The third and fifth columns list the number of candidates in Samples I and II, corrected for detection completeness as per §4.1. Root n error bars can be highly misleading for such small numbers, and so errors are estimated from the Poisson fiducial limits appropriate for small number counts tabulated by Regener (1951). Columns four and six give the surface densities, corrected for detection incompleteness. The cumulative surface density of QSO candidates for $19.3 < m_{606} < 24.0$ —the approximate equivalent of $19.8 \lesssim B \lesssim 24.5$ —is $420^{+180}_{-130} \text{ deg}^{-2}$ for Sample I, or $290^{+160}_{-110} \text{ deg}^{-2}$ for Sample II.

In Figure 7 we plot these cumulative surface densities for our ultrafaint candidates (large filled squares) along with comparison points from other brighter QSO surveys and several predictions of model luminosity functions for $z < 2.1$. The $\log N - \log S$ curve data derived from other brighter low- z QSO surveys (mainly UV-excess) are taken from Hartwick & Schade (1990; hereafter, HS) who compiled data for $\sim 10^3$ confirmed QSOs in the magnitude range $12.5 < B < 22.5$. As discussed above, the somewhat bluer edge of the u^* passband as compared to the Johnson U passband limits the sensitivity of our survey to $z \lesssim 2.1$. We estimate $N(z < 2.1)/N(z < 2.2) \approx 0.96$ by interpolating the redshift distribution of multicolor selected QSOs derived by Koo & Kron (1988), and apply this small correction to the HS compilation data.

The HS $\log N - \log S$ data plotted in Figure 7 rely at their faintest end—overlapping our bright end—especially on the work of Koo and Kron and collaborators (e.g., Koo & Kron 1988). Based on the spectroscopically confirmed QSOs in the Koo & Kron sample in the magnitude range $20.0 < B < 22.6$ at $0 < z < 2.1$, a surface density of about 130 deg^{-2} may be inferred; the number of such QSOs predicted in our survey area using the latter value is then 3.2, and thus in good agreement with the $2.0^{+2.6}_{-1.3}$ such “bright” QSO candidates we actually find (although the numbers

are very small in our sample for such “bright” QSOs). Similar agreement is found at our “bright” end between the observed surface densities of our candidates and measures for confirmed $z \lesssim 2.1$ QSOs in the Canada-France Redshift Survey (Schade et al. 1996) to $B < 23$. The slope of the HS cumulative $\log N - \log S$ relation at the faint end is 0.35 for $\lesssim 2.1$ QSOs. An extrapolation to $B \lesssim 24.5$ of the HS slope predicts for our survey area 14.1 QSOs; this prediction agrees reasonably well with our measure from Sample I candidates of $10.4_{-3.2}^{+4.4}$ (Table 6). Thus, as may be discerned visually from Figure 7, a simple extrapolation of the HS $z < 2.1$ QSO $\log N - \log S$ curve to $B \lesssim 24.5$ appears to also match our observed surface density measure of candidates very well.

A popular model of the QSO luminosity function—at least for faint, low- to moderate- z QSOs—has been that presented by Boyle et al. (1988; hereafter BSP), Boyle (1991), and see also Marshall (1987). They parameterize the luminosity function as a double power law, with a shallow component at low luminosities and a steep component at high luminosities. In the case of pure luminosity evolution, the redshift dependence is often expressed as a power law $L(z) \propto (1+z)^{k_L}$, with $k_L \approx 3.15$. We carry out an integration to $z = 2.1$ of the BSP luminosity function using their best-fit model parameters, and for $q_0=0.5$ and $H_0=50$ (their model B), to predict the $\log N - \log S$ curve for QSOs to $B < 24.5$, and beyond; $B = 24.5$ corresponds to $M_B = -20.9$ at $z = 2.1$ for their model B. The predictions of the BSP luminosity function to $B \lesssim 24.5$ (solid curve in Figure 7) are in good agreement with the observed surface densities of our Sample II candidates. As may also be seen in Figure 7 (dashed curve), similarly good agreement is found between our faint candidate surface densities and the predictions of a Gaussian form of pure luminosity evolution proposed by Pei (1995); the Pei luminosity function fits the available $\log N - \log S$ curve data for brighter confirmed QSOs reasonably well over the entire observed redshift range, even beyond $z > 3$. Lastly, we plot in Figure 7 (dotted curve) the predictions of an example of a physically-based model luminosity function proposed by Yi (1996); the redshift dependence of the QSO luminosity in a low-efficiency advection-dominated regime can be approximated in the Yi model by a standard pure luminosity evolution form, and again there is good agreement between the model predictions (for a plausible QSO formation epoch near $z \approx 3.6$; see Beck-Winchatz 1998 for details) and our ultrafaint $\log N - \log S$ data points in Figure 7.

In summary, as is evident from Figure 7, our surface density of morphologically plus multicolor-selected QSO *candidates* to $m_{606} < 24$ (corresponding approximately to $B \lesssim 24.5$) agrees extremely well with extrapolations to faint magnitudes from a variety of other brighter QSO surveys, as well as with the predictions of several pure luminosity function models, both phenomenological and physically-based.

Finally, we also plot in Figure 7 a new upper limit derived from the Conti et al. (1999) study of even fainter QSO/AGN candidates in the Hubble Deep Field (hereafter HDF). Conti et al. (1999) independently arrive at a combined multicolor and morphological selection approach, although their morphological criteria for resolved QSO/AGNs may not be quite so specifically targeted at QSOs/AGNs with point-source nuclei as that we describe in §3.2. Conti et al. ultimately quote an upper limit to the QSO/AGN surface density at $m_{606} < 27.0$, as their criteria also include

objects having colors consistent with normal stars. Their Tables 4 and 6 list 14 objects they call attention to as potential low- z QSOs or resolved (in WFPC2) AGN candidates which, for the HDF area of 4.4 square arcminutes, corresponds to an upper limit of $<11,500 \text{ deg}^{-2}$ QSOs/AGNs with $m_{606} < 27.0$, corresponding to about $B \lesssim 27.5$. There is no inconsistency between the upper limit inferred from the Conti et al. (1999) data, and a smooth extrapolation from the HS $\log N - \log S$ curve nor with our candidate points corresponding to $B \lesssim 24.5$. It appears possible that some of the low- z candidates in the HDF are not QSOs/AGNs (see additional discussion in Conti et al. 1999), or that a large population of extremely low luminosity QSOs/AGNs has emerged in the HDF.

6. Summary and Conclusions

We have completed a combined multicolor and morphological survey for QSOs to $m_{606} < 24.0$ ($B \lesssim 24.5$) in 0.025 deg^2 of the Groth-Westphal Strip, using $F606W$ and $F814W$ WFPC2 images from HST and u^* -band images from the APO 3.5-m. Objects are selected as QSO/AGN candidates according to their UV-excess (likely $z \lesssim 2.1$), and if they have either stellar morphology, or an approximately stellar-nucleus even if an underlying galaxy is evident, in HST images.

We find 10 high-likelihood QSO/AGN candidates in our survey area which satisfy these criteria (Sample I). We also devise a second sample (Sample II) which excludes three objects from Sample I on the basis of their red ($m_{606} - m_{814}$) color, to potentially further reduce residual contamination by compact galaxies. The cumulative surface density of QSO candidates for $19.3 < m_{606} < 24.0$, the approximate equivalent of $19.8 \lesssim B \lesssim 24.5$, is $420_{-130}^{+180} \text{ deg}^{-2}$ for Sample I, or $290_{-110}^{+160} \text{ deg}^{-2}$ for Sample II. At our “bright” end ($B \lesssim 22.5$) our $\log N - \log S$ relation for candidates agrees well with the surface density of QSOs found by Koo & Kron (1988), Schade et al. (1996), and others. At the faint end, our results are consistent with extrapolations to $B \lesssim 24.5$ of the HS $\log N - \log S$ curve, and the predictions of several recent pure luminosity evolution models (BSP; Pei 1995; Yi 1996). Hence, this pure luminosity evolution description, which has often been argued to provide a good representation of the evolution of QSOs to $B < 22.5$, may be a good description of the evolution of even fainter (low- to modest-redshift) QSOs as well. Note that such good agreement with extrapolations from brighter surveys and model luminosity function predictions need not have been the case: as discussed in §3.2, we would have found nearly an order of magnitude more UV-excess quasar candidates had we used only color information and neglected the morphology information available in HST images.

While it is gratifying that the surface densities derived from our QSO candidates are in good agreement with extrapolations from brighter spectroscopically confirmed QSO samples and model predictions, follow-up of our candidates is of course highly desirable and well within the capabilities of 10m-class telescopes instrumented for multi-object spectroscopy. Spectroscopic confirmations of our candidates as QSOs/AGNs would allow an initial exploration of the ultrafaint luminosity function (and any confirmations of very faint UV-excess white dwarfs would also be

intriguing). Of course, even negative spectroscopic results indicating that the sample candidates are not QSOs/AGNs are potentially of high interest; such results would even more stringently constrain our already low initial estimates of the surface densities of ultrafaint QSOs.

7. Acknowledgments

We thank the University of Washington 3.5-m TAC for generous allocations of observing time, the excellent APO support staff, and C. Stubbs, A. Diercks, P. Doherty, and E. Magnier for their development of and shared expertise on SPIcam. We thank E. Deutsch for creating IDL code used for some of data reductions herein. The Medium-Deep Survey analysis was funded by the HST WFPC2 Team and STScI grants GO2684, GO6951, and GO7536 to Prof. Richard Griffiths and Dr. Kavan Ratnatunga at Carnegie Mellon University. Our work was supported at the University of Washington by NASA/HST grant GO-07976.01-96A, and is based on observations with the NASA/ESA Hubble Space Telescope, obtained at the Space Telescope Science Institute, which is operated by the Association of Universities for Research in Astronomy, Inc., under NASA contract NAS5-26555.

REFERENCES

- Bahcall, J. N., Kirhakos, S., Saxe, D. H., & Schneider, D. P. 1997, *ApJ*, 479, 642
- Beck-Winchatz, B. 1998, Ph.D. Thesis, University of Washington
- Bertin, E., & Arnouts, S. 1996, *A&AS*, 117, 393
- Blandford, R. 1986, in *Quasars: Proc. of the 119th Symp. of the IAU*, ed. G. Swarup & V. K. Kapahi (Dordrecht: Reidel), 359
- Boyle, B. J., Shanks, T., & Peterson, B. A. 1988, *MNRAS*, 235, 935 (BSP)
- Boyle, B. J. 1991, in *The Space Distribution of Quasars*, ASP Conference Series Vol. 21, ed. D. Crampton (San Francisco: ASP), 389
- Brunner, R. J., Connolly, A. J., & Szalay, A. S. 1999, *ApJ*, in press
- Cavaliere & Padovani 1989, *ApJ*, 340, L5
- Conti, A., Kennefick, J. D., Martini, P., & Osmer, P. S. 1999, *AJ*, in press
- Fleming, T. A., Liebert, J., & Green, R. F. 1986, *ApJ*, 308, 176
- Francis, P. J., Hewett, P. C., Foltz, C. B., Chaffee, F. H., Weymann, R. J., & Morris, S. L. 1991, *ApJ*, 373, 465
- Fukugita, M., Ichikawa, T., Gunn, J. E., Doi, M., Shimasaku, K., & Schneider, D. P. 1996, *AJ*, 111, 1748
- Gould, A., Flynn, C., & Bahcall, J. N. 1998, *ApJ*, 503, 798
- Graham, M. J., Clowes, R. G., & Campusano, L. E. 1998, *ApJ*, in press
- Griffiths, R. E. et al. 1994, *ApJ*, 437, 67
- Groth, E. J., Kristian, J. A., Lynds, R., O’Neil, E. J., Balsano, R., Rhodes, J., & the WFPC-1 IDT 1994, *BAAS*, 26, 1403
- Gunn, J. E., & Stryker, L. 1983, *ApJS*, 52, 121
- Haiman, Z., & Menou, K. 1999, *ApJ*, submitted
- Hall, P. B., Osmer, P. S., Green, R. F., Porter, A. C., & Warren, S. J. 1996, *ApJ*, 462, 614
- Hansen, B., 1998, *Nature*, 394, 860
- Hartwick, F. D. A., & Schade, D. 1990, *ARAA*, 28, 437 (HS)
- Holtzman, J. A., Burrows, C. J., Casertano, S., Hester, J. J., Trauger, J. T., Watson, A. M., & Worthey, G. 1995, *PASP*, 107, 1065
- Hooper, E. J., Impey, C. D., & Foltz, C. 1997, *ApJ*, 480, L95
- Hutchings, J. B., Holtzman, J., Sparks, W. B., Morris, S. C., Hanisch, R. J. 1994, *ApJ*, 429, L1
- Jarvis, R. M. & MacAlpine, G. M. 1999, *AJ*, in press
- Kennefick, J. D., Osmer, P. S., Hall, P. B., & Green, R. F. 1997, *AJ*, 114, 2269

- Koo, D. C., Kron, R. G. & Cudworth, K. M. 1986, *PASP*, 98, 285
- Koo, D. C., & Kron, R. G. 1988, *ApJ*, 325, 92
- Koo, D. C., et al. 1996, *ApJ*, 469, 535
- Liebert, J., Dahn, C. C., & Monet, D. G. 1988, *ApJ*, 332, 891
- Malkan, M. A., Gorjian, V., & Tam, R. 1998, *ApJS*, 117, 25
- Marshall, H. L. 1987, *AJ*, 94, 628
- Osmer, P. S., Kennefick, J. D., Hall, P. B., & Green, R. F. 1998, *ApJS*, in press
- Pei, Y. C. 1995, *ApJ*, 438, 623
- Ratnatunga, K. U., Griffiths, R. E., & Ostrander E. J. 1999, in preparation
- Regener, V. H. 1951, *Phys. Rev.*, 84, L161
- Roche, N., Ratnatunga, K., Griffiths, R. E., Im, M., & Neuschaefer, L. 1996, *MNRAS*, 282, 1247
- Sarajedini, V. L., Green, R. F., Griffiths, R. E., & Ratnatunga K. U. 1996, *ApJ*, 471, L15
- Sarajedini, V. L., Green, R. F., Griffiths, R. E., & Ratnatunga K. U. 1999a, *ApJS*, in press
- Sarajedini, V. L., Green, R. F., Griffiths, R. E., & Ratnatunga K. U. 1999b, *ApJ*, in press
- Schade, D., Crampton, D., Hammer, F., Le Fevre, O., & Lilly, S. J. 1996, *MNRAS*, 278, 95
- Schmidt, M. & Green, R. F. 1983, *ApJ*, 269, 352
- Veron, P. 1983, in *Quasars and Gravitational Lenses*, Proc. of the 24th Liege International Astrophysical Colloquium, ed. J. P. Swings (Liège: Univ. de Liège), 210
- Warren, S. J., Hewett, P. C., Irwin, M. J., McMahan, R. G., Bridgeland, M. T. , Bunclark, P. S. , & Kibblewhite, E. J. 1987, *Nature*, 325, 131
- Whitmore, B. 1995, in *Calibrating Hubble Space Telescope: Post Servicing Mission*, ed. A. Koratkar & C. Leitherer (Baltimore: STScI), 269
- Yi, I. 1996, *ApJ*, 473, 645

Table 1. UV-Excess (& Misc. High- z) QSO Candidates with Stellar-PSFs in WFPC2

Cat. ID	RA (14:)	Dec (+52:)	m_{606} (Aper)	$u^* - m_{606}$ (Aper)	$m_{606} - m_{814}$ (Aper)	Stellarity	Comments
98	15:30.49	04:39.9	19.88	0.59	0.36	0.89,0.90	UV-excess
971	16:13.41	11:36.3	20.60	0.41	0.37	0.98,1.00	UV-excess
815	16:29.00	15:33.0	23.61	-0.14	0.46	0.98,1.00	UV-excess
245	17:28.35	28:13.3	23.91	-0.09	0.66	0.99,0.92	UV-excess
1082	15:42.65	09:27.6	21.21	2.31	0.22	1.00,1.00	high- z ?
1702	16:53.98	20:43.4	23.57	>2.05	0.34	1.00,0.98	high- z ?

Note. — Column 1 - our catalog ID number; Columns 2 & 3 - J2000 coordinates; Column 7 - SExtractor stellarity in F606W,F814W.

Table 2. UV-Excess QSO Candidates, Approx. Stellar-Nuclei in WFPC2

Cat. ID	RA (14:)	Dec (+52:)	m_{606} (MDS)	$u^* - m_{606}$ (MDS)	$m_{606} - m_{814}$ (MDS)	$\frac{I_{RAD},}{\frac{R_{MAJ}}{R_{MIN}}}$
72	15:39.39	04:44.5	23.90	0.50	0.47	0.39,1.32
1148	15:51.93	08:30.5	23.78	0.32	0.79	0.27,1.11
1025	16:09.02	10:50.9	23.32	0.44	0.43	0.41,1.19
507	16:53.28	21:03.8	22.69	0.26	1.23	0.39,1.09
608	16:55.00	18:38.5	23.78	0.15	0.53	0.49,1.09
315	17:14.41	25:46.4	23.18	0.18	0.30	0.40,1.24
390	17:19.32	23:13.2	22.79	0.70	0.48	0.41,1.23

Note. — Column 1 - our catalog ID number; Columns 2 & 3 - J2000 coordinates; Column 7 - WFPC2 radial profile integral, major-to-minor axis ratio.

Table 3. Miscellaneous Compact UV-Excess Objects (Too Extended or Too Faint)

Cat. ID	RA (14:)	Dec (+52:)	m_{606} (MDS)	$u^* - m_{606}$ (MDS)	$m_{606} - m_{814}$ (MDS)	$I_{RAD},$ $\frac{R_{MAX}}{R_{MIN}}$	Comments
1233	15:14.74	01:37.6	23.62	0.38	0.41	0.56,1.27	slight extension
1176	15:15.88	03:27.0	24.06	-0.14	0.67	0.45,1.24	$m_{606} > 24$
802	16:22.65	15:07.5	23.94	0.30	0.36	0.56,1.12	slight extension
757	16:36.54	16:49.9	23.60	0.11	0.77	0.60,1.01	slight extension
505	16:51.34	20:46.1	21.37	0.21	0.41	0.57,1.07	face-on host
359	17:10.90	23:46.6	23.88	0.63	0.54	0.77,1.94	tidal tail?
163	17:54.64	30:57.0	23.20	-0.07	0.76	0.67,1.42	edge-on host?

Note. — Column 1 - our catalog ID number; Columns 2 & 3 - J2000 coordinates; Column 7 - WFPC2 radial profile integral, major-to-minor axis ratio; Column 8 - comments (mainly on visual appearance in WFPC2).

Table 4. Summary Information for QSO Candidates in Combined UV-Excess Sample I

Obj. No.	Cat. ID	RA (14:)	Dec (+52:)	m_{606} (Aper)	Stellarity	MDS Class	$I_{RAD},$ $\frac{R_{MAX}}{R_{MIN}}$	Comments
1	98	15:30.49	04:39.9	19.88	0.89,0.90	0,3	0.21,1.12	obvious host
2	1148	15:51.93	08:30.5	23.83	0.61,0.34	0,1	0.27,1.11	
3	1025	16:09.02	10:50.9	23.31	0.77,0.37	0,2	0.41,1.19	obvious host
4	971	16:13.41	11:36.3	20.60	0.98,1.00	0,0	0.01,1.23	
5	815	16:29.00	15:33.0	23.61	0.98,1.00	0,0	—	nearby spiral
6	507	16:53.28	21:03.8	22.93	1.00,0.04	2,2	0.39,1.09	fuzz in F814W
7	608	16:55.00	18:38.5	23.87	0.27,0.06	1,1	0.49,1.09	
8	315	17:14.41	25:46.4	23.29	0.03,0.04	1,1	0.40,1.24	
9	390	17:19.32	23:13.2	22.79	0.56,0.44	0,2	0.41,1.23	fuzz;close star?
10	245	17:28.35	28:13.3	23.91	0.99,0.92	2,2	0.49,1.23	fuzz? in F814W

Note. — Column 1 - QSO candidate no. in Beck-Winchatz (1998); Column 2 - our catalog ID number; Columns 3 & 4 - J2000 coordinates; Column 6 - SExtractor stellarity in F606W,F814W; Column 7 - MDS morphological class; Column 8 - WFPC2 radial profile integral, major-to-minor axis ratio; Column 9 - comments on visual appearance in WFPC2.

Table 5. Object Detection Probabilities for SPICam Images

u^*	2nd Deepest Field	2nd Shallowest Field	Typical Value
23.0-23.5	0.97	0.94	0.97
23.5-24.0	0.96	0.92	0.96
24.0-24.5	0.91	0.78	0.83
24.5-24.7	0.61	0.41	0.49

Table 6. Cumulative Surface Densities of QSO Candidates

m_{606}	B	n Sample I	N (deg ⁻²) Sample I	n Sample II	N (deg ⁻²) Sample II
23.0	23.5	$5.0^{+3.4}_{-2.2}$	210^{+140}_{-90}	$3.0^{+3.0}_{-1.6}$	120^{+120}_{-70}
23.5	24.0	$7.1^{+3.8}_{-2.6}$	290^{+160}_{-110}	$5.1^{+3.4}_{-2.2}$	210^{+140}_{-90}
24.0	24.5	$10.4^{+4.4}_{-3.2}$	420^{+180}_{-130}	$7.2^{+3.8}_{-2.6}$	290^{+160}_{-110}

Note. — Columns 3 & 5 - cumulative number of QSO candidates in survey region, corrected for detection incompleteness; Columns 4 & 6 - cumulative surface density of QSO candidates, corrected for detection incompleteness.

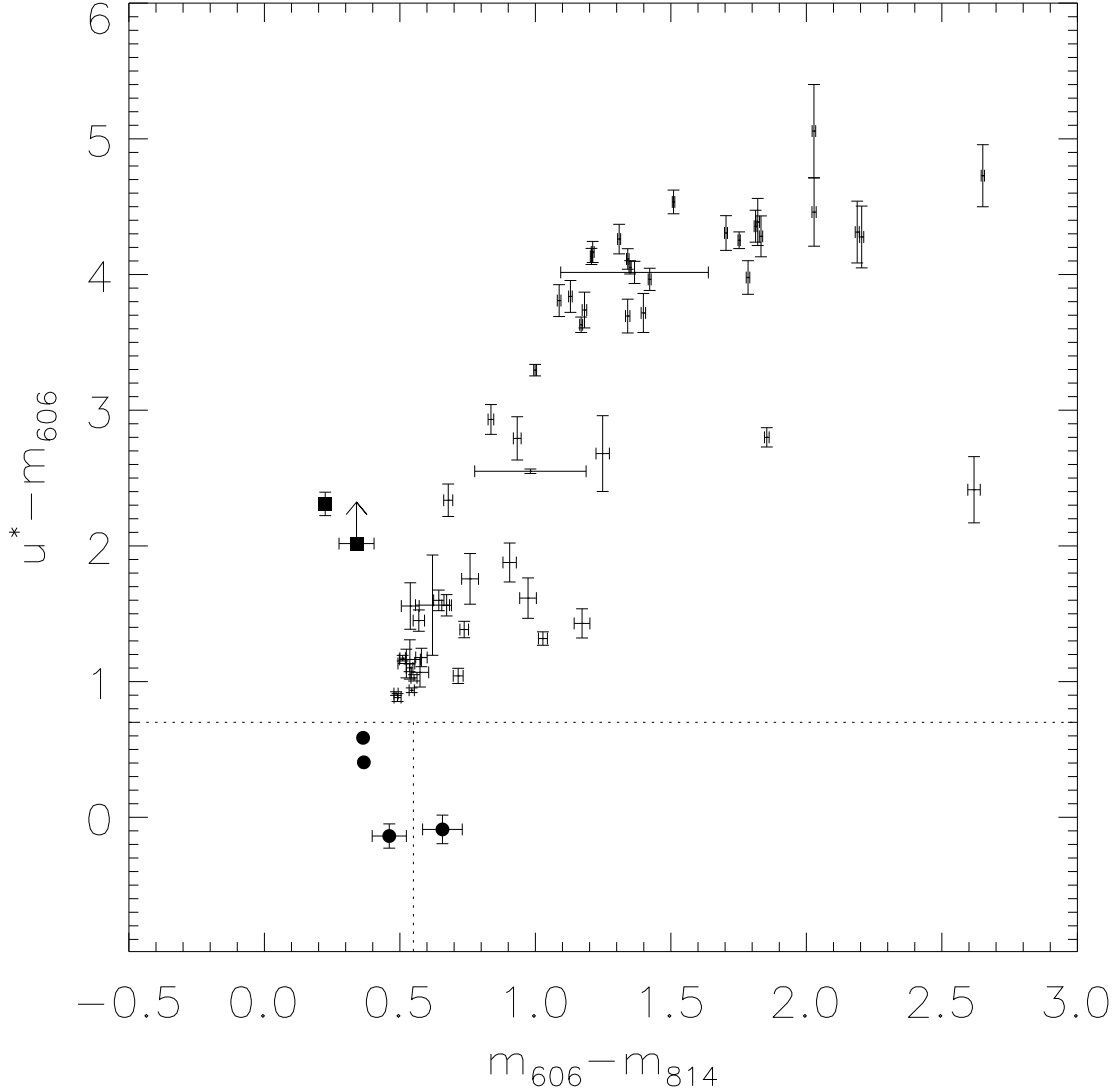


Fig. 1.— Two-color diagram of objects (1σ photometric errors) in our survey to an aperture magnitude limit of $m_{606} < 24$, that were classified as having stellar morphology in WFPC2 by the SExtractor neural network. For added clarity, we do not plot u^* non-detections (with one exception). Filled circles denote the four UV-excess quasar candidates (see also Table 1) with stellar-PSF morphology in WFPC2 (for two of these candidates, the photometric errors are merely smaller than the plot symbol). The dotted horizontal and vertical lines indicate, respectively, our UV-excess criterion and an additional possible $(m_{606} - m_{814})$ color-cut to further exclude compact emission line galaxies. The filled squares denote two miscellaneous higher redshift QSO candidates (see Table 1).

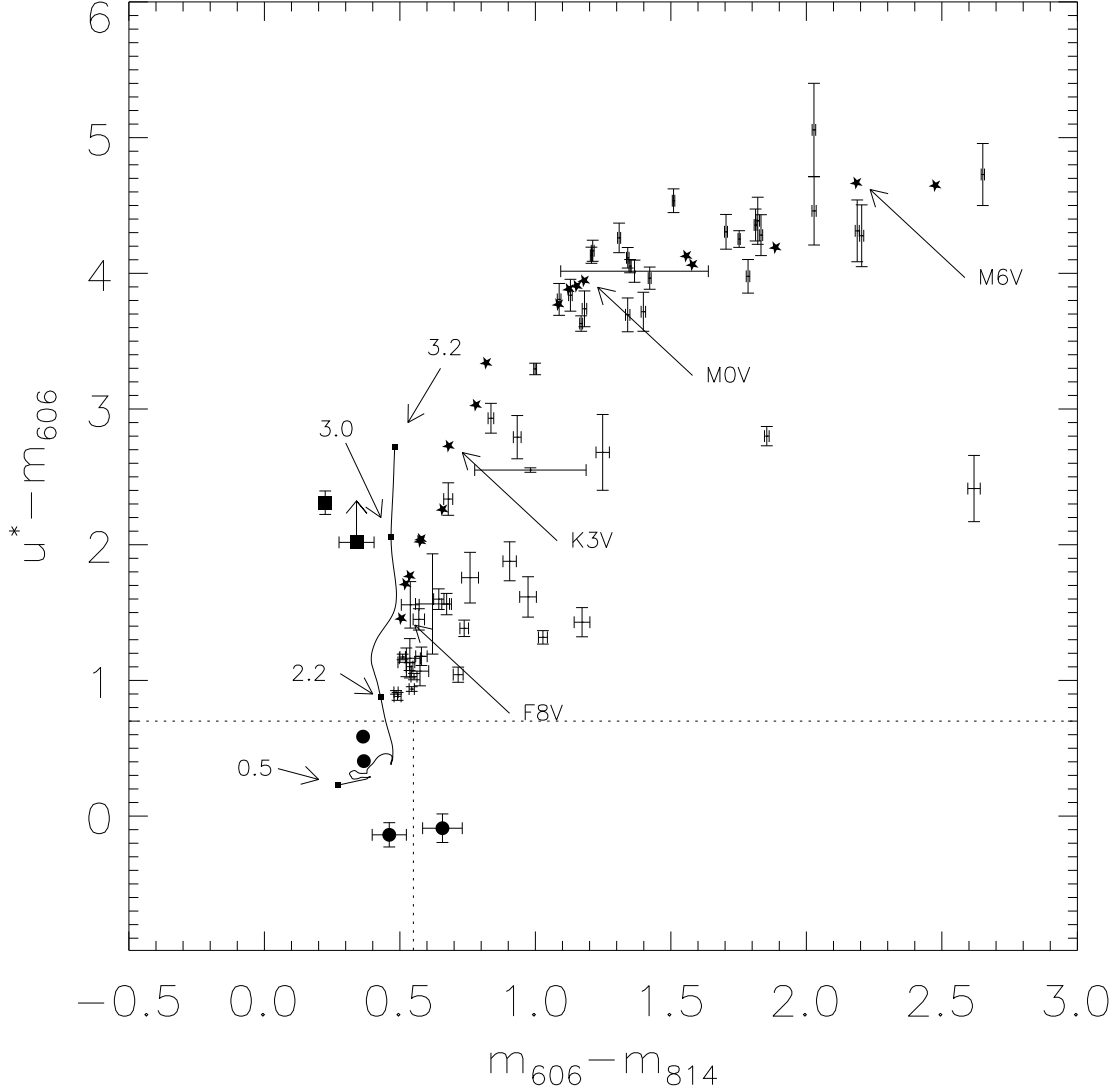


Fig. 2.— Two-color diagram of stellar-PSF (in WFPC2) objects in our survey to an aperture magnitude limit of $m_{606} < 24$. Data and symbols are identical to those shown in Figure 1, except that we also overplot for rough comparison the locus of colors expected of a typical quasar at various redshifts (solid curve), and the approximate colors predicted for main sequence stars (5-point star symbols) later than spectral type F8.

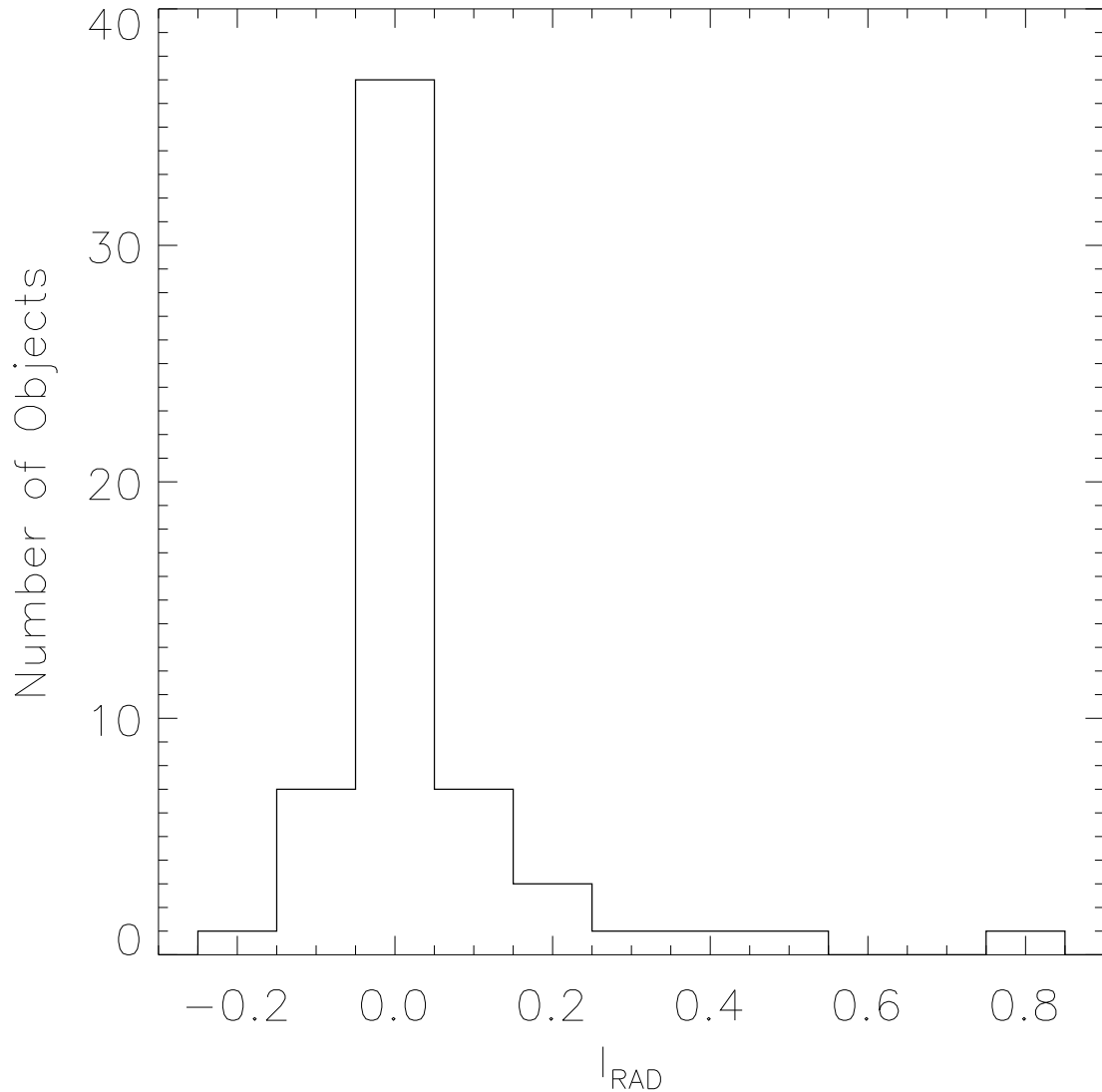


Fig. 3.— Histogram of radial profile integrals, I_{RAD} , for WFPC2 objects having stellar-PSFs according to SExtractor (distribution of I_{RAD} for objects plotted in Figure 1). As nearly all such stellar-PSF in WFPC2 objects have $I_{RAD} < 0.5$, we also invoke this criterion as one portion of a dual quantitative test to assess whether UV-excess galaxies resolved in WFPC2 images, nonetheless have an approximately stellar-PSF nucleus, and hence may be high likelihood QSO/AGN candidates.

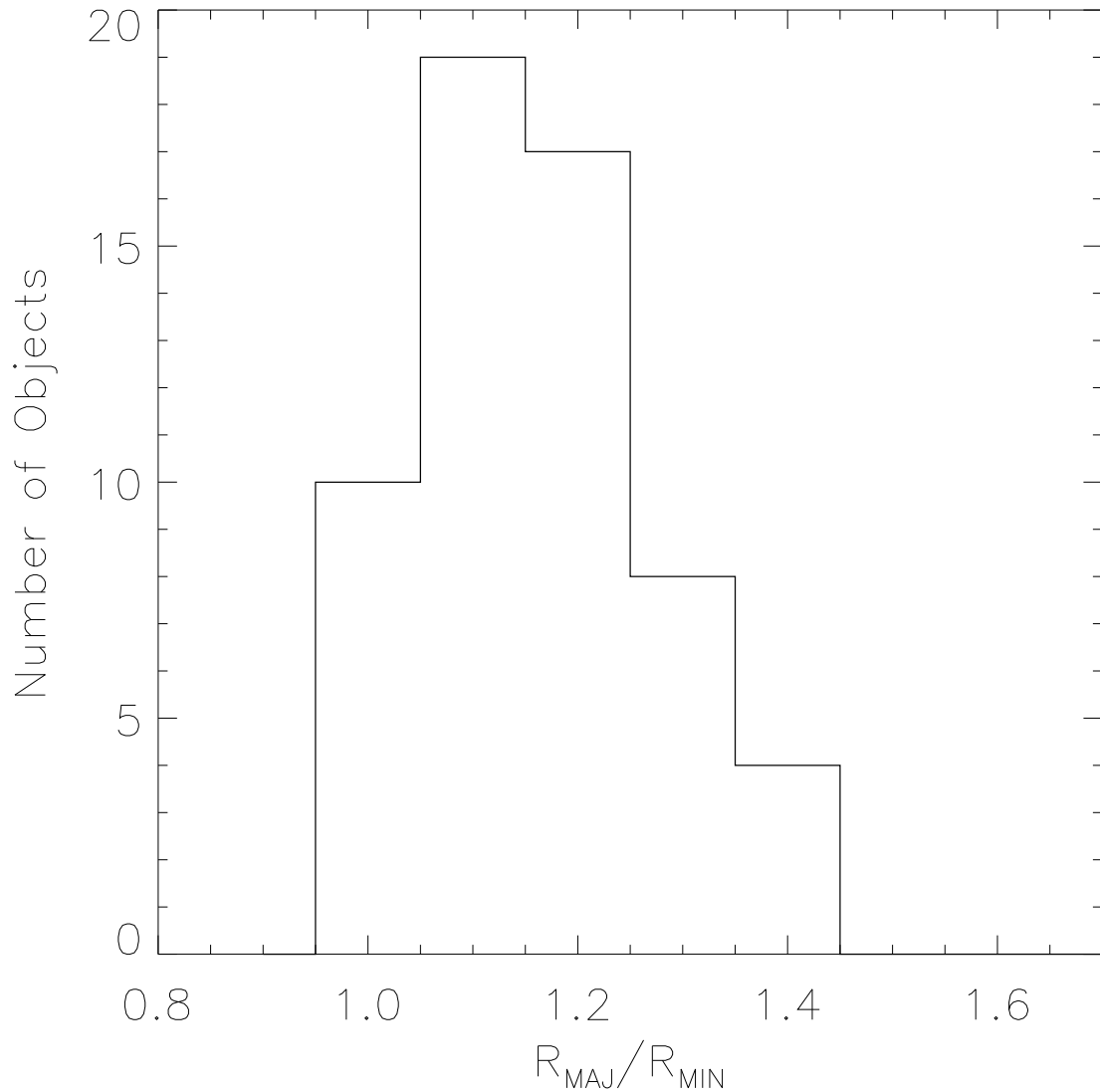


Fig. 4.— Histogram of the major to minor axis ratios (R_{MAJ}/R_{MIN}) of two-dimensional elliptical Gaussian fits to WFPC2 objects having stellar-PSFs according to SExtractor (distribution of R_{MAJ}/R_{MIN} for objects plotted in Figure 1). As all such stellar-PSF in WFPC2 objects have $R_{MAJ}/R_{MIN} < 1.5$, we also invoke this criterion as the second portion of a dual quantitative test to assess whether UV-excess galaxies resolved in WFPC2 images, nonetheless have an approximately stellar-PSF nucleus, and hence may be high likelihood QSO/AGN candidates.

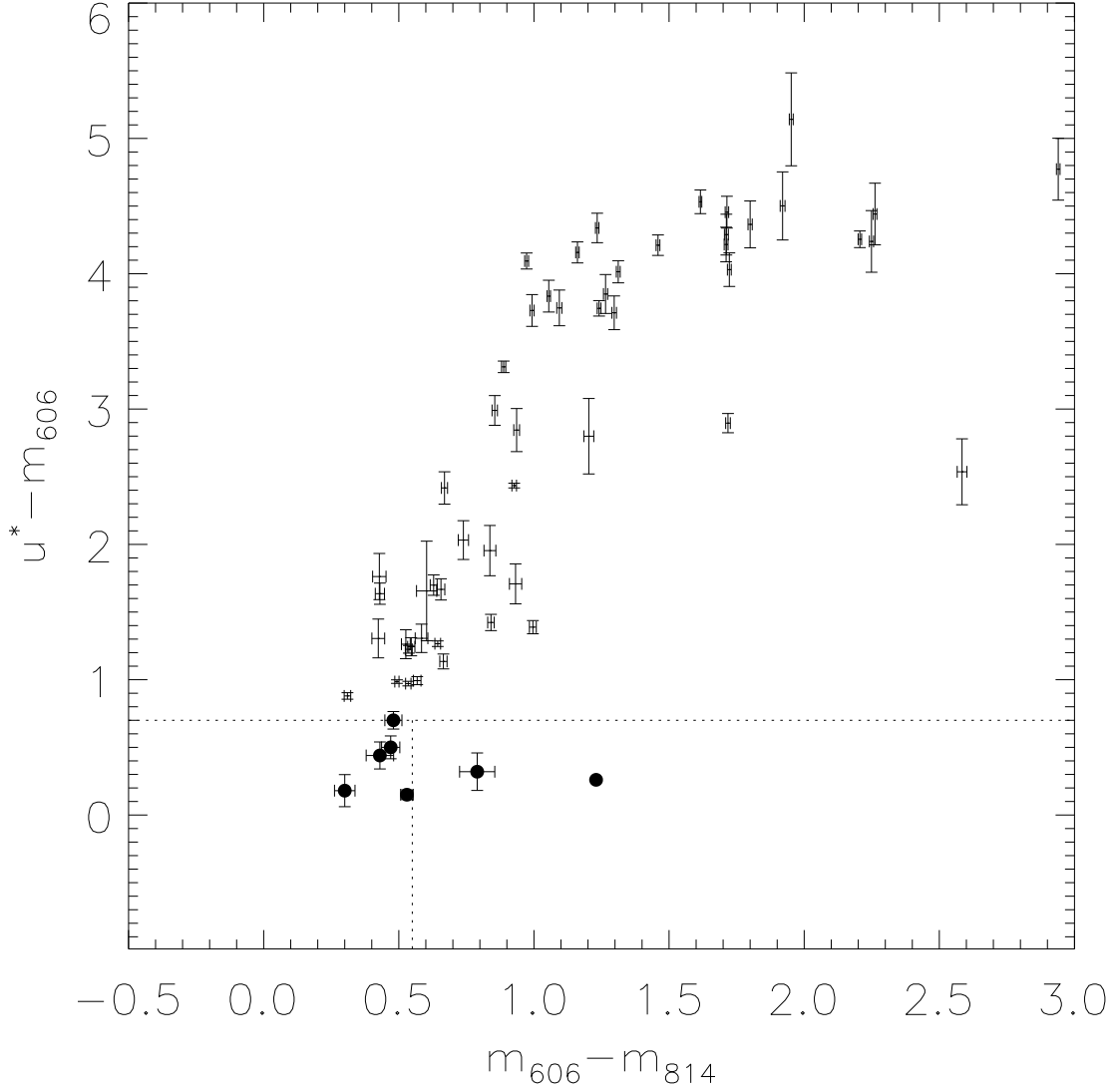


Fig. 5.— Two-color diagram of objects (1σ photometric errors) in our survey to an MDS magnitude limit of $m_{606} < 24$. Error bars denote colors of objects classified as having stellar-PSF morphology in WFPC2 by the MDS algorithm (but otherwise this figure is analogous to Figure 1). The filled circles overplot the colors of additional UV-excess QSO/AGN candidates (see Table 2) that have stellar-nuclei+galaxy morphology. (QSO candidates already plotted in Figures 1–2 and listed in Table 1 are *not* replotted here).

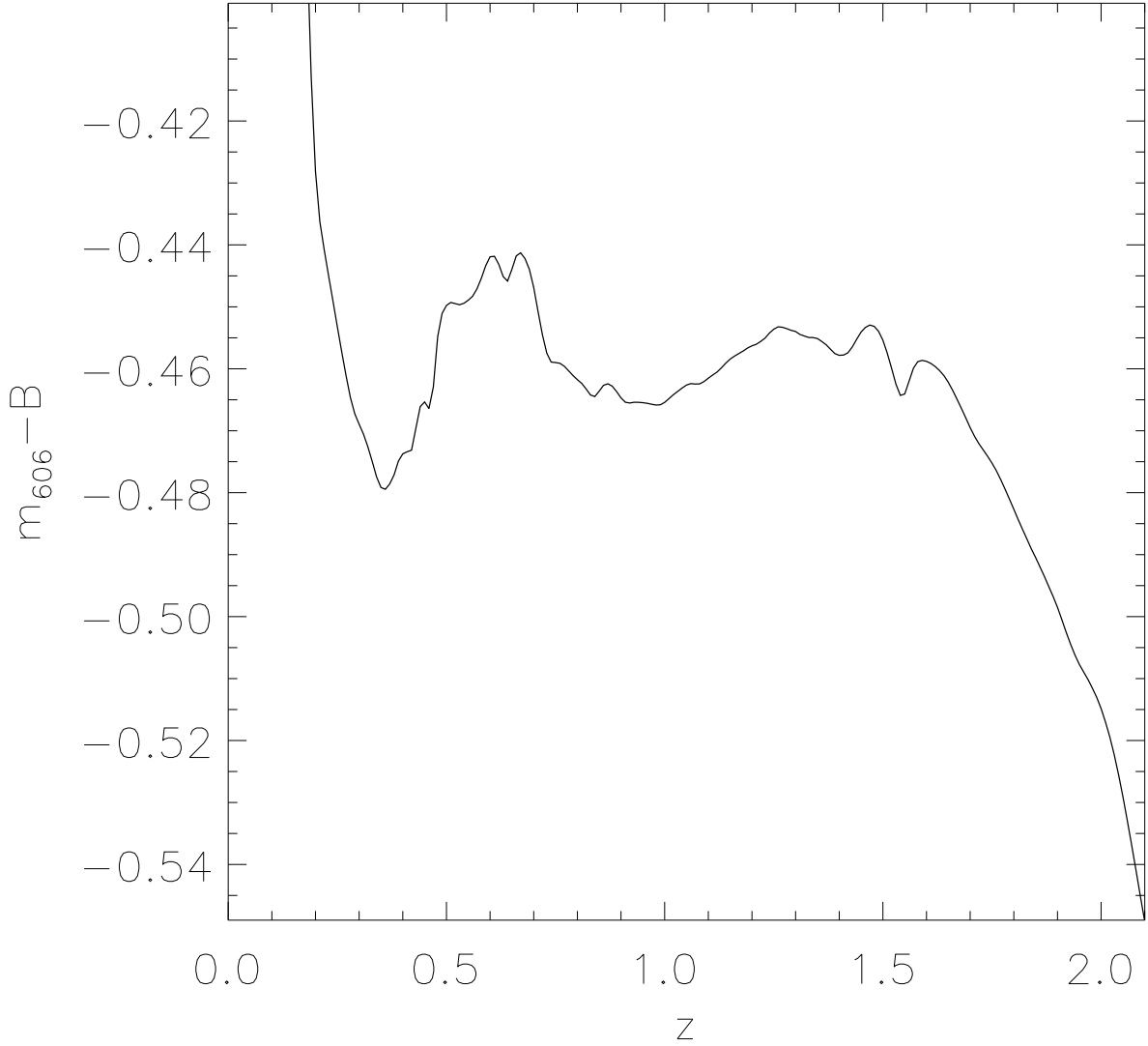


Fig. 6.— A rough conversion, as a function of redshift, between the $F606W$ magnitude (including the contribution of emission lines) of a typical QSO and the Johnson B -band continuum magnitude. This was estimated by convolving the redshifted composite LBQS spectrum, as well as a cubic spline fit to its continuum, with the wavelength dependent sensitivity curves of the HST/WFPC2/ $F606W$ system and the B -band. The LBQS spectrum is defined for $\lambda \leq 6000 \text{ \AA}$ and does not completely overlap the $F606W$ bandpass for $z \lesssim 0.2$; this causes the sharp increase in $(m_{606} - B)$ at low redshifts. For very approximate comparison with the results of other quasar surveys defined in terms of B -band magnitudes, we adopt $B \approx m_{606} + 0.5$ as typical for $z < 2.1$ QSOs.

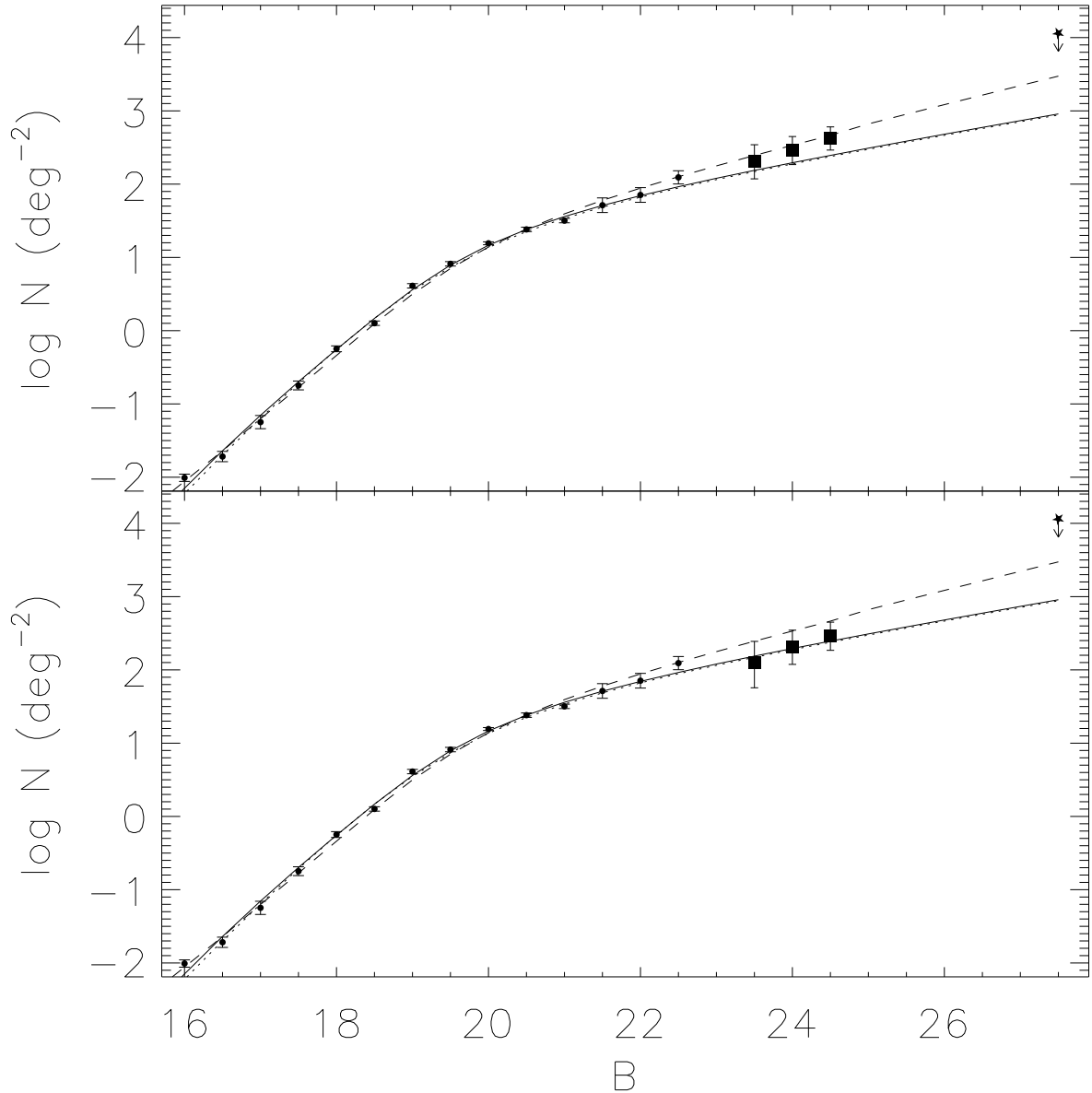


Fig. 7.— Comparison of cumulative surface densities of QSO/AGN candidates (squares) from Sample I (upper panel) and Sample II (lower panel) with the predictions of three pure luminosity evolution models for $z < 2.1$. Solid curves show the predictions of a double power-law luminosity function combined with the power-law pure luminosity evolution given by BSP. Dashed curves show the predictions of a Gaussian pure luminosity evolution of Pei (1995), which fits even higher- z QSO data as well. Dotted curves show the predictions of a physically based model by Yi (1996). Also plotted (small circles) are the surface densities of confirmed brighter QSOs derived by HS, as well as an upper limit (arrow at $B \approx 27.5$) on extremely faint low- z QSOs from the HDF (Conti et al. 1999). Excellent agreement is found between the surface density of QSO candidates in our samples to $B \lesssim 24.5$, predictions of pure luminosity evolution models, and simple extrapolations from brighter surveys.